Interaction of Bragg scattering band gaps and local resonators in mono-coupled periodic structures

Mattia Cenedese,[1] Edoardo Belloni,[2] and Francesco Braghin[2, a)]
[1)] *Institute for Mechanical Systems, ETH Zürich, Leonhardstrasse 21, 8092 Zürich, Switzerland*
[2)] *Department of Mechanical Engineering, Politecnico di Milano, Via La Masa 1, 20156 Milano, Italy*

(Dated: February 9, 2021)

Periodic structures have gained attention in the research community since they show attenuation zones in their frequency response, called band gaps. In this paper, the interactions of two mechanisms of band gap formation in mono-coupled periodic structures are examined, i.e., Bragg scattering and local resonators. With reference to longitudinal elastic waves, an analytical study is carried out to describe in detail the formation of band gaps. Local resonators are implemented via piezoelectric inserts shunted with a resonating electrical circuit, for which a non-traditional model is needed since the study concerns higher frequencies with respect to those of the subwavelength regime. Design maps and tuning formulas are developed not only for the case of infinite structure, but also for the finite case, highlighting the role of the number of unit cells and that of resonances in the attenuation zones. Among the possible tuning strategies of local resonators, it is shown that the mutual influence between elastic and electric parameters is able to produce a wider attenuation zone, bridging Bragg scattering band gaps thanks to the effect of local resonators. The analytical findings of this paper are validated with numerical results in an example application.

I. INTRODUCTION

A periodic structure consists of a number of identical structural components (called unit cells) which are joined together end-to-end and/or side-by-side to shape the whole structure. This geometry allows creating frequency intervals in which an incident wave is not transmitted, broadly known as band gaps. Thanks to this dynamic property, they have raised a considerable interest in several research fields like structural vibrations and acoustics[1,2], phononics[3–5], photonics[6], phoXonics[7,8] and electron or plasma waves[9,10]. In the context of structural vibrations, a band gap is caused by a number of different phenomena. Bragg scattering was the first to be analyzed[11]: when waves encounter a periodic change in the propagating medium, diffraction takes place provided that the spatial periodicity of the perturbation is close to a multiple of the wavelength[12–15]. Another cause of band gaps are localized resonant structures. These typically show up a band gap at a wavelength well below the Bragg scattering one (i.e., the so-called subwavelength regime). There is a consistent literature about purely mechanical local resonant structures (see for example[16–19]), but also a significant number of publications deals with smart materials used as local resonators (see[20–22]). Other techniques rely on mode coupling[23], hybridization[4,24] or time-modulation[25,26]. To further enhance properties of periodic media, recent studies consider the coexistence of Bragg scattering and local resonators[27–37]. In particular, Kaina et al.[29], Yuan et al.[31], Krushynska et al.[35] and Moscatelli et al.[37] report that, in different applications, the local resonators can widen and strengthen the Bragg scattering band gaps.

In mono-dimensional periodic structures wave propagation occurs along a single direction. The degree of coupling is equivalent to half the number of boundary conditions needed for solving the wave partial differential equation of the medium[38]. In this work, mono-coupled periodic structures are considered, in particular the paper refers to the case of longitudinal wave propagation in rods[39,40]. However, several of the obtained concepts and formulas could also be applied to other physical models, such as transversal vibrations in strings[38], surface acoustic wave mono-dimensional devices[41,42], torsional vibrations of shafts[43,44] and transversal vibrations in periodically supported beams[45]. In this study, the Bragg scattering is generated by an impedance mismatch between two different elements that make up the unit cell, while local resonators are implemented with piezoelectric inserts shunted with a resonating electrical circuit[46–48]. The most common applications exploit local resonators to create a low frequency band gap, before the occurrence of Bragg scattering. However, these literature models of shunted piezoelectric inserts or patches are no longer valid at the frequencies where Bragg scattering takes place[49], i.e., where the local resonators can interact with Bragg scattering band gaps.

Mono-dimensional, linear periodic structures present the analytical advantage of having a closed form solution of the wave propagation problem. Among the large variety of methods developed for the study of periodic structures[2,13], the transfer matrix method[50–52] is chosen in this paper, since it allows to describe the wave propagation behavior of the whole structure just based on the characteristics of the unit cell. Indeed, the transfer matrix links the state vector of subsequent unit cells and it is a symplectic linear map, a property that has several implications among which a significant simplification of computations[45,53,54]. To determine how waves propagate, it is sufficient to study the eigenvalues of the transfer matrix (analogue to the imposition of Bloch-Floquet conditions[55,56]), thus the attention is focused on the transfer matrix invariants[57,58]. These latter depend on a number of non-dimensional parameters, therefore it is possible plot the system behavior in design maps presenting a clear understand-

[a)] Electronic mail: francesco.braghin@polimi.it

ing of the physical phenomena involved.

The typical design of periodic structures is based on the analysis of the wave propagation behavior. However, this dynamics is valid for an infinite medium, while in the finite systems are characterized by standing waves. Analytical relations for propagation in finite structures would be notably useful to investigate how the number of unit cells influences the system behavior[59–61]. This is influence is not limited to the attenuation level in band gaps, but also on resonances, that depend on boundary conditions and topological configurations of the periodic structure.

This paper studies the interactions between Bragg scattering and local resonators band gaps in mono-coupled periodic structures. Based on the transfer matrix method, design maps and tuning guidelines via analytic formulas are derived both for the infinite and finite propagating media, which is uncommon in available literature results. Specifically, the transmissibility ratio is introduced and exploited for characterizing finite periodic systems. Here, the structural design needs to consider not only band gaps, but also the number of unit cells and potential resonances that may break the attenuation zones of band gaps. Local electromechanical resonators are introduced via a new modeling of piezoelectric elements, which is valid for frequencies above for subwavelength regime. There are three possibilities for tuning the intrinsic band gap of local resonators: before the Bragg scattering band gaps (as in traditional metamaterials), inside a band gap in order to break it or in between two Bragg scattering band gaps. In this latter case, it is possible to make a bridge between two Bragg scattering band gaps through the resonators effect for generating an extra wide attenuation zone. With respect to available literature results on interactions between Bragg and local resonant band gaps, we develop a detailed parametric analysis, and we highlight the role of metadamping.

The article is developed in four main sections. First, the dynamics of mono-coupled periodic structures is summarized both for infinite and finite systems. In Sec. III, we discuss structures whose band gaps are generated via Bragg scattering only, providing design maps and close-form tuning formulas. Section IV introduces resonant shunted piezoelectric inserts along the periodic structure and analyzes the coupling of Bragg scattering and local resonator band gaps. The last section presents a numerical application of the bridging effect of local resonators on two Bragg scattering band gaps, which validates the analytical tuning predictions presented in this paper.

II. DYNAMICS OF MONO-COUPLED PERIODIC STRUCTURES

The typical mono-coupled periodic structure and its unit cell are illustrated in Fig. 1, with reference to the case of periodic rods. The linear, longitudinal wave propagation, at frequency ω, in a homogeneous rod element is governed by the wave equation in the frequency domain[62]

$$\frac{d^2u}{dx^2}+\frac{\omega^2}{c_{el}}u=0, \tag{1}$$

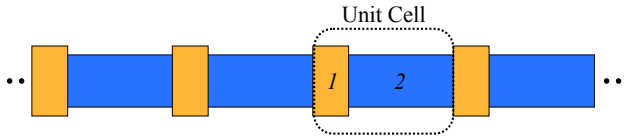

Figure 1. Representation of the periodic rod and the selection of the unit cell.

where $u(x)$ is the displacement field, $c_{el}=\sqrt{Y_{el}/\rho_{el}}$ the wave speed for the rod element, ρ_{el} its density and Y_{el} its Young's modulus. The wavenumber κ_{el} is defined as ω/c_{el}, while A_{el} indicates the cross section. A unit cell, marking the spatial periodicity of the structure, is made-up by stacking different rod elements and its length is denoted l_c. Using the notation f for the longitudinal force, the two-dimensional state vector $\underline{y}^{(n)}=[u(nl_c)\ f(nl_c)]^T$ describes displacement and force at a location in the n-th unit cell. State vectors of subsequent unit cells are related by the transfer matrix $[T(\omega)]$ as

$$\underline{y}^{(n+1)}=[T(\omega)]\underline{y}^{(n)}. \tag{2}$$

The transfer matrix of the unit cell, which is assembled from the transfer matrices of single elements, plays a key role in uncovering the dynamics of the structure both in the infinite and in the finite cases. A detailed derivation for the rod case is presented in Appendix A. By definition, it must be symplectic[53,54], which implies that $\det([T(\omega)])=1$ always and that any eigenvalue appears in couple with its reciprocal. Thus, λ_i is an eigenvalue of $[T(\omega)]$, also $1/\lambda_i$ is an eigenvalue of $[T(\omega)]$. In the case of mono-coupled systems (2×2 transfer matrix), only one couple exists. Note that, even though the transfer matrix changes for different unit cell discretizations of the structure with fixed spatial periodicity l_c, its eigenvalues are invariant as discussed in Appendix A.

Wave propagation in the infinite medium can be studied via Floquet-Bloch conditions[11,55,63], i.e., imposing that $\underline{y}^{(n+1)}=\lambda\underline{y}^{(n)}$, where $\lambda=e^{\mu}$ is the so-called Floquet multiplier and μ is known as the propagation constant. The Floquet-Bloch condition states that Floquet multipliers coincide with the eigenvalues of the transfer matrix, i.e., $[T(\omega)]\underline{y}=\lambda\underline{y}$. Therefore, if μ is purely imaginary, then $|\lambda|=1$ and a wave can freely propagate (pass band). If μ has a real part, $|\lambda|\neq 1$, thus a wave is attenuated when $|\lambda|<1$ (stop band or band gap) or amplified when $|\lambda|>1$ (in non-active structures, this does not happen due to energy conservation). As pointed out by[56], for a m-coupled system there are m couples of waves, for which $\lambda\leftrightarrow-\mu$ and $1/\lambda\leftrightarrow+\mu$ are forward and backward propagating waves respectively.

In the case of longitudinal wave propagation, a single type of wave exists $m=1$, whose dispersion relation reads[39,45,64]

$$\mu=\mu(\omega)=\operatorname{acosh}\left(\frac{\operatorname{Tr}([T(\omega)])}{2}\right). \tag{3}$$

Equation (3) is the fundamental equation to study wave propagation in mono-coupled structures and it is exploited in the upcoming sections. The dynamical behavior is only dependent on the trace of the transfer matrix, its first invariant.

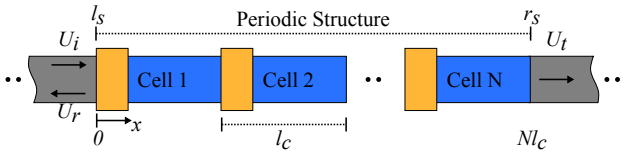

Figure 2. Representation of wave propagation in a finite periodic rod.

A finite periodic structure requires a different approach, but the transfer matrix $[T(\omega)]$ is still the key ingredient. The general behavior of a finite periodic structure can be analyzed by adopting the configuration shown in Fig. 2, which is typical in optics[65]. Here, a finite periodic rod made up by N cells is inserted in an infinite and continuous rod made of another material (referred as external medium).

Generally speaking, when an incident wave U_i, propagating from left to right, arrives at the boundary of a periodic structure, part of this wave is reflected back (U_r), while the remaining part is transmitted through the periodic structure (U_t). Now, it is possible to introduce the transmissibility ratio t as the ratio between the transmitted wave over the incident one (there is also a reflection ratio r, i.e., the ratio between reflected and incident waves). Reasonably, t is somehow related to the pass/stop band nature of the periodic structure. If μ is a relevant indicator for wave propagation in infinite periodic structures, in finite periodic structures of N unit cells there is a similar quantity named α, the attenuation coefficient (per element), that is related to t as

$$|t| = e^{-\alpha N}, \quad \alpha = -\log(|t|)/N. \tag{4}$$

The spectral analysis of the waves propagating in the external medium gives

$$\begin{gathered} u_i(x) = U_i \mathrm{e}^{-j\kappa_e x} \quad , \quad u_r(x) = U_r \mathrm{e}^{+j\kappa_e x} \\ u_t(x) = U_t \mathrm{e}^{-j\kappa_e (x - N l_c)}, \end{gathered} \tag{5}$$

where U_i, U_r and U_t are complex values, j is the imaginary unit and the subscript e indicates the properties of the external material. By using the notation

$$[T(\omega)] = \begin{bmatrix} t_{11} & t_{12} \\ t_{21} & t_{22} \end{bmatrix}, \tag{6}$$

and indicating with $z_e = Y_e A_e / c_e$ the impedance of the external medium, the next result characterizes the transmissibility ratio.

Proposition II.1. *The transmissibility ratio $t = U_t/U_i$ is characterized by the following formula*

$$t = \frac{2}{\left[-(t_{11} - t_{22}) + j \left(\omega z_e t_{12} + \dfrac{t_{21}}{\omega z_e} \right) \right] \dfrac{\sinh(N\mu)}{\sinh(\mu)}}. \tag{7}$$

This result is proven in Appendix B. Here, it is also shown that, for an infinite number of elements, the attenuation per element α converges to

$$\lim_{N\to\infty} \alpha = \lim_{N\to\infty} \frac{-\log|t|}{N} = \mathrm{Re}(\mu), \tag{8}$$

as expected. Moreover, a closed form expression exists also for the reflection ratio $r = U_r/U_i$ (see Appendix B). The formula in Eq. (7) replaces the dispersion relation in Eq. (3) to analyze wave propagation in finite periodic media and the dependence on the number of unit cells can be clearly identified.

III. DESIGN OF BRAGG BAND GAPS

This section aims to study the case of the periodic rod whose band gaps are generated via Bragg scattering only. This periodic rod and the selected unit cell are represented in Fig. 1. This latter is made up by two different rod elements and it is selected in an asymmetric fashion.

A. Infinite structure

The transfer matrix for a rod element considering a compressive longitudinal force reads

$$[T_{el,k}] = \begin{bmatrix} \cos(\kappa_k l_k) & \dfrac{\sin(\kappa_k l_k)}{z_k \omega} \\ -z_k \omega \sin(\kappa_k l_k) & \cos(\kappa_k l_k) \end{bmatrix} \tag{9}$$

where $z_k = Y_k A_k / c_k = A_k \sqrt{Y_k \rho_k}$ is the rod element characteristic impedance for $k = 1, 2$, as shown in Appendix A 1. The unit cell in Fig. 1 is made up by two different rod elements, therefore the whole transfer matrix for the unit cell is

$$[T] = [T_{el,2}][T_{el,1}] \tag{10}$$

where $[T_{el,1}]$ is the transfer matrix of the first part (at the left side of the unit cell) and $[T_{el,2}]$ the transfer matrix of the second part (at the right side). The trace of the transfer matrix $\mathrm{Tr}([T(\omega)]) = I_1$, i.e., its first invariant, takes the form

$$\begin{aligned} I_1 = \; & 2\cos(\kappa_1 l_1)\cos(\kappa_2 l_2) + \\ & - \sin(\kappa_1 l_1)\sin(\kappa_2 l_2) \left(\frac{z_2}{z_1} + \frac{z_1}{z_2} \right). \end{aligned} \tag{11}$$

Being I_1 always real in this case, a simple analysis of Eq. (3) shows that the propagation constant is purely imaginary if $-2 \le I_1 \le 2$. Outside this interval μ has a real part, so that there exists a band gap and no wave can propagate along the structure. In case of undamped mono-coupled systems, only pure pass ($\mathrm{Re}(\mu) = 0$) and stop bands ($\mathrm{Re}(\mu) \neq 0$) exist.

As pointed out by Ref. 57, it is convenient to express the invariants as a function of a set of non-dimensional parameters to obtain a useful tool for periodic structure design. The simplest set for the periodic rod case is

$$\zeta = \frac{z_2}{z_1} = \frac{A_2 \sqrt{Y_2 \rho_2}}{A_1 \sqrt{Y_1 \rho_1}}, \quad \Lambda = \frac{\kappa_2 l_2}{\kappa_1 l_1} = \frac{c_1 l_2}{c_2 l_1}, \quad \Omega = \frac{\omega l_1}{c_1}, \tag{12}$$

where ζ is the ratio of impedances (representing the internal impedance mismatch), Λ is a ratio between lengths and propagation speeds, Ω is the non-dimensional frequency. Furthermore,

$$\omega_{m,k} = m\pi \frac{c_k}{l_k}, \quad f_{m,k} = \frac{m}{2} \frac{c_k}{l_k}, \quad k = 1, 2, \; m \in \mathbb{N} \tag{13}$$

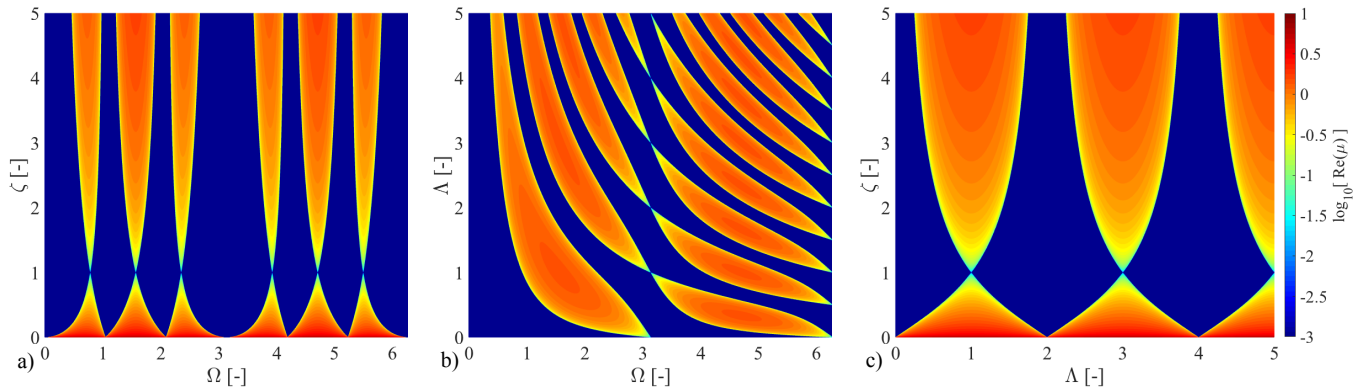

Figure 3. Non-dimensional maps obtained by the invariant equation. Color-scale represents the level of attenuation, quantified using the logarithm of the real part of the propagation constant. a) $\Omega-\zeta$ map with $\Lambda=3$; b) $\Omega-\Lambda$ map with $\zeta=4$; c) $\zeta-\Lambda$ map with $\Omega=\pi/2$.

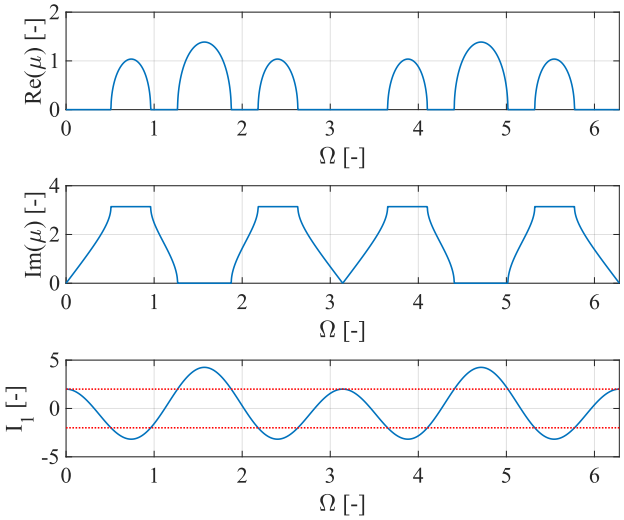

Figure 4. Propagation constant μ and first invariant I_1 trends in Ω for $\zeta=4$ and $\Lambda=3$. In the plot of I_1, the two red dotted lines show the values ± 2.

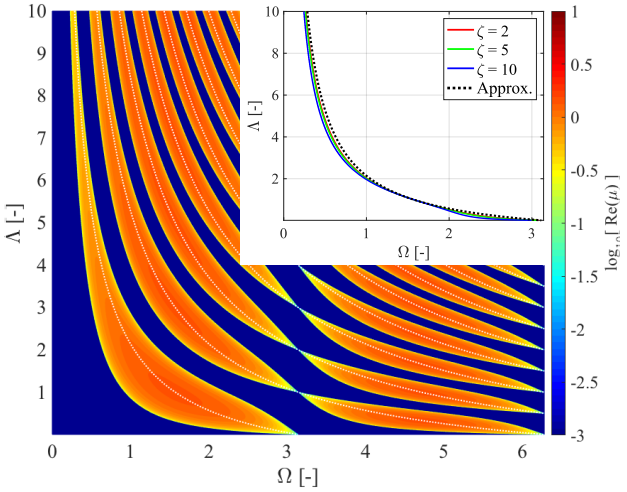

Figure 5. $\Omega-\Lambda$ map at $\zeta=4$ with the approximated band gap center locations and, in the small upper right plot, approximated first band gap location Ω_c ($m=1$, dotted line) against the actual ones for different internal impedance mismatch values indicated by the colored lines.

are the natural frequencies either for free-free or clamped-clamped boundary conditions for element 1 and element 2. When Ω is equal to $m\pi$ we are in coincidence of a natural frequency of element 1. Instead, Λ is the ratio between correspondent natural frequencies of element 1 and 2 respectively.

With some substitutions and manipulations, the first invariant can be written as

$$\begin{aligned} I_1 = \; & 2\cos(\Omega)\cos(\Lambda\Omega)-\sin(\Omega)\sin(\Lambda\Omega)\left(\zeta+\frac{1}{\zeta}\right) \\ = \; & \left[1+\left(\frac{\zeta}{2}+\frac{1}{2\zeta}\right)\right]\cos[\Omega(1+\Lambda)]+ \\ & +\left[1-\left(\frac{\zeta}{2}+\frac{1}{2\zeta}\right)\right]\cos[\Omega(1-\Lambda)], \end{aligned} \tag{14}$$

thus $I_1=I_1(\zeta,\Lambda,\Omega)$. Figure 4 shows the dispersion plot for a unit cell having $\zeta=4$ and $\Lambda=3$.

Fixing one of the non-dimensional parameters, it is possible to plot the design maps in Fig. 3 that represent how pass and stop bands change as a function of the other non-dimensional parameters. While deep blue represents pass band, the color scale shows the wave attenuation in logarithmic values. Focusing now on the $\Omega-\zeta$ map of Fig. 3a, it holds that:

- since ζ appears in the trace as $\hat{\zeta}(\zeta)=\zeta+1/\zeta$, it is possible to analyze just the interval $0<\zeta<1$ or the one $\zeta>1$ since the functions $\hat{\zeta}(\zeta)$ and $\hat{\zeta}(1/\zeta)$ have the same images. As ζ departs from 1 the attenuation level and the width of the band gaps increases, while no stop band is present for $\zeta=1$;
- if $\Lambda\in\mathbb{Q}$, then the I_1 is a periodic function in Ω and consequently pass/stop bands will have a periodic trend along frequencies, cf. Fig. 4 where the period is π;
- a band gap attenuation is symmetric in frequency with respect to its center where there is the maximum of the real

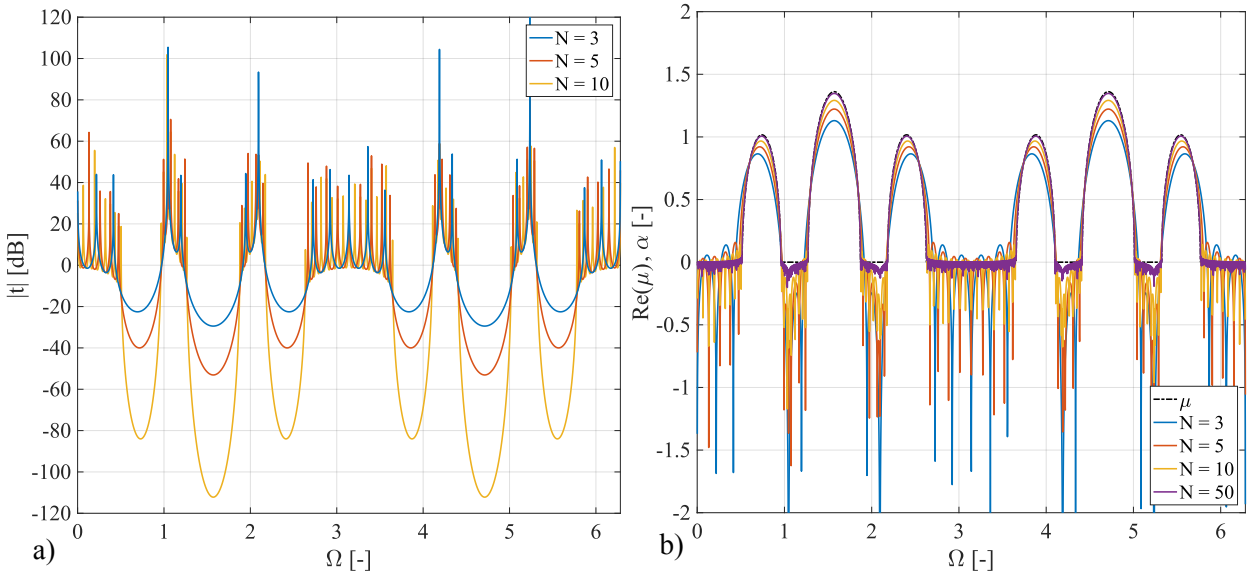

Figure 6. a) Transmissibility ratio in dB and b) attenuation per element α and real part of the propagation constant μ plots with $\zeta = 4$ and $\Lambda = 3$ for different numbers of unit cells: blue line, $N = 3$; orange, $N = 5$; yellow, $N = 10$; purple, $N = 50$ for plot b).

part. The frequency locations of the band gaps centers seem independent from the internal impedance mismatch ζ.

On the other hand, the $\Omega - \Lambda$ map of Fig. 3b shows that:

- the band gap center is strongly affected by the Λ parameter, while this latter has only a modest influence on the amplitude level;
- the number of band gaps in a π period of Ω is equal to the upper rounded integer of Λ;
- The frequencies at which Ω is a multiple of π are always pass ones. From the physic point of view, it means that a wave that passes through element 1 keeps the same amplitude with the same phase or opposite, so element 1 does not contribute to the wave propagation at these frequencies. Analogue considerations hold when $\Lambda\Omega$ is a multiple of π.

Figure 3c shows the influence of both mechanical parameters at a fixed Ω, thus providing information about the robustness of a specific frequency but losing the notion about bandwidth.

From a design point of view, it is valuable to have an analytical formula for the band gap tuning. Accurate information may be derived via numerical studies, but the m-th band gap central frequency Ω_c is approximated as

$$\Omega_c = \frac{m\pi}{1+\Lambda}. \tag{15}$$

The exact derivation of this result is reported in Appendix C and its predictions are shown in Fig. 5. Here, the $\Omega - \Lambda$ map has been integrated with the approximated band gap center locations and, in the inset, the approximated first band gap location Ω_c ($m = 1$, dotted line) is plotted against the actual ones, for some internal impedance mismatch values.

B. Finite structure

For the unit cell selected in Sec. III A in the finite setting of Sec. II and for an external medium with the same material properties of element 1 (i.e., $z_e = z_1$), the transmissibility ratio t takes the form

$$t = -\frac{2j}{U_{N-1}h}e^{-j\Omega},$$
$$h = \left(\frac{1}{\zeta} - \zeta\right)\sin(\Lambda\Omega), \quad U_{N-1} = \frac{\sinh(N\mu)}{\sinh(\mu)}. \tag{16}$$

With respect to the non-dimensional parameters affecting wave propagation, the transmissibility ratio has the additional dependence on the number of unit cells N, i.e., $t = t(\Omega, \zeta, \Lambda, N)$. In Fig. 6, the quantities $|t|$ and α are reported for a periodic structure made up by unit cells having $\zeta = 4$, $\Lambda = 3$ and $z_e = z_1$. Different colors show different number of unit cells.

First, it is clear from Fig. 6a that the number of elements strongly affects the response of the system, both in terms of resonances and of band gap attenuation. From a design point of view, it is therefore possible to define a certain threshold value, a desired reduction in the response, to properly choose the necessary number of unit cells that allows to obtain a desired attenuation in the stop band.

Then, the term $U_{N-1}(\mu)$ is a Chebyshev polynomial of second kind[66]. This function does not have zeros or turning points in the domain range $[1, \infty)$ and the same applies to $(-\infty, -1]$, while it has $N-1$ zeros in the interval $(-1, 1)$. Therefore, when $\mathrm{Tr}([T])$ lays between $(-2, 2)$ there is a pass band, and each pass band is characterized by $N-1$ natural frequencies. On the other hand, h is responsible for the remaining countable infinity of resonances, matching the classic vibration theory. Furthermore, the term h also depends on the

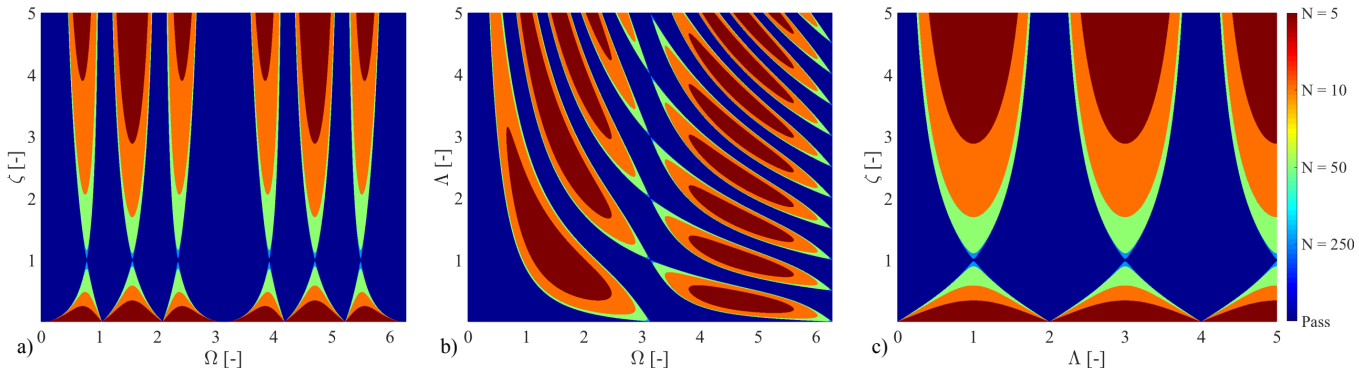

Figure 7. Non-dimensional maps for the finite periodic structure using the transmissibility ratio for a threshold attenuation level of -40 dB. Colors indicate the behavior for different number of unit cells: a) $\Omega-\zeta$ map with $\Lambda=3$; b) $\Omega-\Lambda$ map with $\zeta=4$; c) $\zeta-\Lambda$ map with $\Omega=\pi/2$.

external medium and may also interfere with the Bragg scattering, setting a resonance peak in between a band gap. This case has to be handled with care, as reported in Appendix D.

The design maps computed for the infinite system can be extended for the finite case. In order to evaluate how a stop band evolves with the variation of a non-dimensional parameter, it is necessary to fix a desired attenuation level (a threshold). Figure 7 is obtained for a desired attenuation level of 10^{-2} or -40 dB. The diagrams show pass (in blue) and stop (with various colors depending on the number N of unit cells) bands as function of the considered parameters. It can be noticed that the greater the impedance mismatch, the lower the number of elements necessary to obtain the desired attenuation level. As the band gaps do not change, the formula derived for the location of a band gap center is still valid also in the finite case.

To fully clear the design of a finite periodic system, the application-dependent, finite structural response needs also to be checked and the transfer matrix can be again be exploited for analytical computations, as reported in Appendix D. For instance, by imposing forced-free boundary conditions to the finite periodic rod of Fig. 2, a frequency response function of interest is the transmittance t_r, i.e., the ratio between the displacement of one side and the applied force of the other side. In Fig. 8 the modulus of the transmittance $\bar{t}_r$ is reported in its non-dimensional form for a periodic structure made up by unit cells having $\zeta=4$ and $\Lambda=3$ where different colors show the behavior different number of unit cells. Other than the difference in natural frequencies and the increasing attenuation as the number of unit cells grows, the presence of resonances that breaks the band gaps can be noticed. These resonances, actually corresponding to natural frequencies of the last unit cell, can either ruin band gap attenuation, or exploited to retain only a precise frequency within a stop band.

IV. SHUNTED PIEZOELECTRIC PERIODIC ROD

The presence of a shunted piezoelectric element (often abbreviated with piezo or PZT) in a unit cell of a periodic structure is analyzed in this section. First, the modeling of the piezoelectric domain is presented. Shunted piezoelectric elements are often used to generate a band gap before the appearance of Bragg scattering, but in our formulation the model is substantially renewed since we aim to investigate what happens at higher frequencies[49]. Indeed, the deformation of the element is supposed to be constant in the subwavelength regime, while at higher frequencies this approximation is not valid anymore. Subsequently, the shunted piezoelectric rod element is inserted in the periodic structure of Sec. III, hence driving the analysis on the coexistence of Bragg scattering and local resonator band gaps.

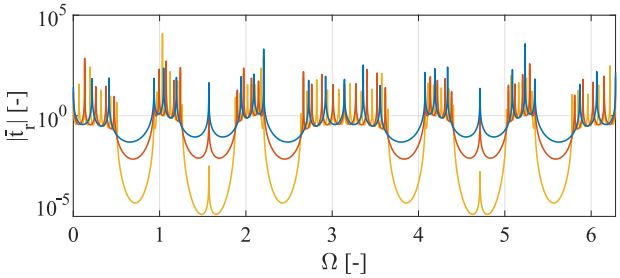

Figure 8. Non-dimensional transmittance modulus of the forced-free finite periodic rod with $\zeta=4$ and $\Lambda=3$ for different numbers of unit cells: blue line, $N=3$; orange, $N=5$; yellow, $N=10$.

A. Element modeling

To obtain the transfer matrix for the $R-L$ shunted piezoelectric bar element shown in Fig. 9a, it is necessary to couple the mechanical and electrical dynamic equations with the piezoelectric constitutive laws. Assuming to directly be in the frequency domain, for what regards mechanics, the infinitesimal equilibrium states[62]

$$\frac{df}{dx}=-\rho A\omega^2 u, \tag{17}$$

with the usual meaning of the parameters. As typically

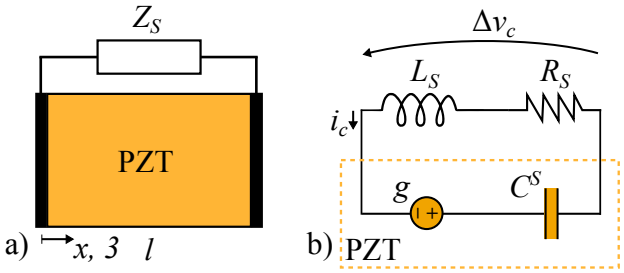

Figure 9. a) Representation of the Shunted Piezoelectric Rod Element; b) Equivalent lumped electrical circuit.

done in literature[46,47,67,68], the electrical circuit is modeled in the lumped parameters fashion since the characteristic wavelength of mechanical vibration is much shorter than the electric field wavelength in piezoelectric materials. Thus, the equation for the electric shunt circuit represented in Fig. 9b is

$$\Delta v_c = -Z_S i_c \quad \rightarrow \quad \Delta v_c = -j\omega Z_S q_c, \tag{18}$$

where i_c is the circuit current, q_c the electrical charge on the electrodes surfaces, $Z_S = R_S + j\omega L_S$ the circuit electric impedance (R_S resistance and L_S inductance) and v_c the potential difference between them. Referring to[69] for the modeling of a 1D piezoelectric element and assuming a pure 33 operating mode (the subscript will be omitted in formulas), the linear constitutive law is

$$\begin{cases} S = \dfrac{T}{Y^E} + dE, \\ D = dT + \varepsilon^T E, \end{cases} \quad \text{or} \quad \begin{cases} T = Y^D S - gD, \\ E = -gS + \dfrac{1}{\varepsilon^S} D, \end{cases} \tag{19}$$

where T is the applied stress, S the strain, E the electric field, D the electrical displacement, Y^E and Y^D the Young's moduli in short circuit condition ($E = 0$) and open circuit condition ($D = 0$) respectively, ε^T and ε^S the electric permittivities at $T = 0$ (stress free condition) and at $S = 0$ (strain free condition) respectively, d the piezoelectric strain coefficient and g the piezoelectric stress coefficient. The piezoelectric coupling coefficient k (or k_{33}), which quantifies the electromechanical energy conversion, satisfies

$$k^2 = d^2 \frac{Y^E}{\varepsilon^T} = g^2 \frac{\varepsilon^S}{Y^D}, \quad \begin{aligned} Y^E &= Y^D(1-k^2), \\ \varepsilon^S &= \varepsilon^T(1-k^2). \end{aligned} \tag{20}$$

Then, it is necessary to integrate the constitutive law in the piezoelectric material volume. First, it is recalled that

$$S = \frac{du}{dx}, \quad f = \int_A T dA, \quad E = \frac{dv_c}{dx}, \quad q_c = \int_A D dA, \tag{21}$$

and, assuming that S and E are uniform along the cross section A (i.e., electrodes surface), Eq. (19) is integrated in the cross section resulting in

$$\begin{cases} f = Y^D A \dfrac{du}{dx} - g q_c, \\ \dfrac{dv_c}{dx} = -g \dfrac{du}{dx} + \dfrac{1}{\varepsilon^S A} q_c. \end{cases} \tag{22}$$

The second equation of Eq. (22) has to be integrated in the longitudinal direction as well

$$\int_0^l \frac{dv_c}{dx} dx = -g \int_0^l \frac{du}{dx} dx + \frac{1}{\varepsilon^S A} \int_0^l q_c dx, \tag{23}$$

while for the two first integrals the result is trivial, the charge needs a further hypothesis: no free charge is assumed inside the piezoelectric material, so Gauss's law states that $\operatorname{div} \underline{D} = 0$. Since that no polarization, field or charge is present in the transversal directions, it is possible to get that (usual hypotheses of mono-dimensional modeling[70])

$$\frac{\partial D}{\partial y} = \frac{\partial D}{\partial z} = 0 \quad \rightarrow \quad \frac{\partial D}{\partial x} = 0 \quad \rightarrow \quad \frac{dq}{dx} = 0, \tag{24}$$

and the charge is thus constant along the x direction. So, Eq. (23) becomes

$$C^S \Delta v_c - q_c = -g C^S \left(u(l) - u(0) \right), \tag{25}$$

where $C^S = \varepsilon^S A / l$ is the strain free piezoelectric capacitance. Note that Eq. (25) represents the PZT highlighted area of the electric circuit illustrated in Fig. 9b. After using here Eq. (18) and isolating q_c, the constitutive law of the $R-L$ shunted PZT bar element takes the form

$$\begin{aligned} &f = Y^D A \frac{du}{dx} - \frac{k^2 Y^D A}{G(\omega)} \frac{u(l) - u(0)}{l}, \quad \omega_{LC,S}^2 = \frac{1}{L_S C^S}, \\ &G(\omega) = 1 + 2\xi j \frac{\omega}{\omega_{LC,S}} - \frac{\omega^2}{\omega_{LC,S}^2}, \quad \xi = \frac{R_S C^S}{2} \omega_{LC,S}, \end{aligned} \tag{26}$$

where $\omega_{LC,S}$ is the electrical shunting frequency and ξ quantifies the electrical damping ratio. The circuit influence depends on the difference of the displacements of the two electrodes that is actually what the lumped parameter circuit can sense. Thus, when the displacements of the electrodes are in phase with the same amplitude, the shunt does not affect the dynamics, while if they are out of phase, its effect is maximum.

Typically, $R-L$ shunted PZT elements are used in the subwavelength regime[46,49,68], for which

$$\frac{u(l) - u(0)}{l} \approx \frac{du}{dx} \quad \rightarrow \quad f = Y^D A \left(1 - \frac{k^2}{G(\omega)} \right) \frac{du}{dx}, \tag{27}$$

where the piezoelectric effect is enclosed into the Young's modulus. Approaching the first Bragg scattering band gap, the subwavelength hypothesis is not valid, so the force expression of Eq. (26) is adopted instead of that in Eq. (27).

By further analyzing the circuit equation (18) and the function $G(\omega)$, three main frequency regions can be distinguished for the behavior of the $R-L$ shunted PZT:

- $\omega \rightarrow 0$: short circuit behavior. Indeed, from the circuit equation, the electrical field is almost null here and the shunting circuit is practically a short circuit. The piezo elastic modulus can be approximated with Y^E;
- $\omega \rightarrow \infty$: open circuit behavior. Here, $G(\omega)$ tends to infinity as well and the charge is basically null. So, the piezo elastic modulus reveals to be Y^D;

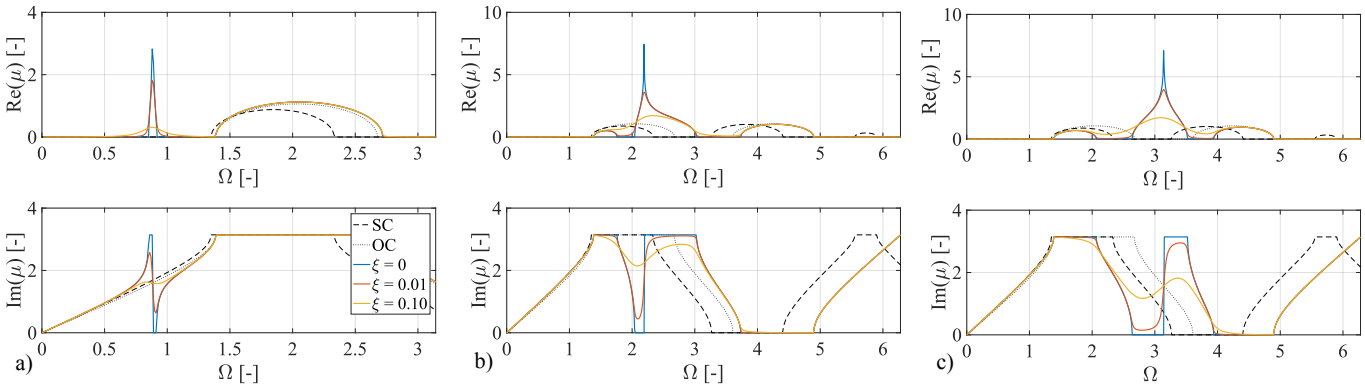

Figure 10. Dispersion plot of the $R-L$ shunted PZT periodic structure with $\zeta = 0.3$, $\Lambda = 0.5$ and $k = 0.5$: a) Tuning A, $\Omega_{LC,S} = 1$; b) Tuning B, $\Omega_{LC,S} = 2.3$; c) Tuning C, $\Omega_{LC,S} = \pi$. The blue line is for $\xi = 0$; the orange one for $\xi = 0.01$, the yellow one for $\xi = 0.10$, the black dashed one illustrates the short circuit response (SC) and the black dotted line the open circuit one (OC).

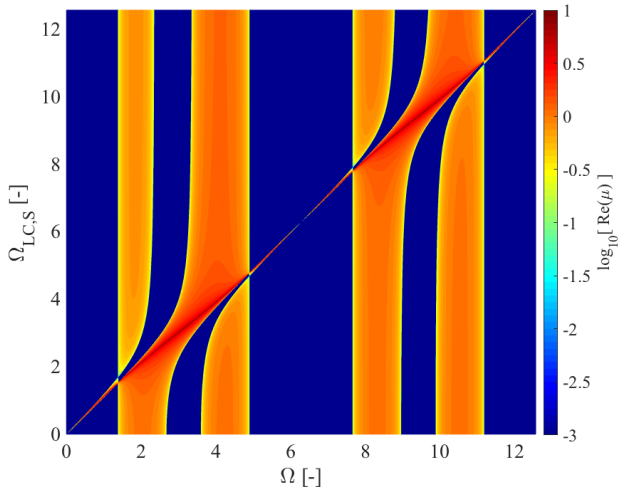

Figure 11. Non-dimensional $\Omega - \Omega_{LC,S}$ map where color-scale represents the level of attenuation, quantified using the logarithm of the real part of the propagation constant. The other non-dimensional parameters are selected as follows: $k = 0.5$, $\zeta = 0.3$, $\Lambda = 0.5$ and $\xi = 0$.

- $\omega \to \omega_{LC,S}$: resonant zone. Considering $\xi = 0$, $G(\omega)$ tends to 0 and provides a resonating trend to the piezo dynamic stiffness. In particular, an attenuation zone rises up and it is called intrinsic band gap since it is a property of the material and it is independent on Bragg scattering or other periodic behaviors. This phenomenon has its physical motivation on the inductor: near the resonance frequency the inductor is effectively accumulating the energy coming from the mechanical domain. This argument is still valid also in presence of a resistance which introduces energy dissipation in the system reducing the attenuation peak and spreading the resonator contribution in frequency.

Since the electric term in Eq. (26) does not depend on x, the differentiation here brings to

$$\frac{df}{dx} = Y^D A \frac{d^2u}{dx^2} \tag{28}$$

that, coupled with Eq. (17), gives again Eq. (1) with $c = c^D = \sqrt{Y^D/\rho}$. Therefore, following the modeling steps of Appendix A but considering Eq. (26) in the context of Eq. (A2), the dynamic stiffness matrix here is found to have an additional shunting term with respect to its purely mechanical one $[K_{el}(\omega)]$, i.e.,

$$[K_{PZT}(\omega)] = [K_{el}(\omega)] + \frac{Y^D A}{l}\frac{k^2}{G(\omega)}\begin{bmatrix} +1 & -1 \\ -1 & +1 \end{bmatrix}, \tag{29}$$

and, using Eq. (A5) it is possible to compute the transfer one.

B. Coupling Bragg scattering with electromechanical resonators

The reference configuration is depicted in Fig. 1 where the medium 1 is the shunted PZT element. Using the notation

$$\Omega = \kappa_1^D l_1 = \frac{\omega l_1}{c_1^D} = \omega l_1 \sqrt{\frac{\rho_1}{Y_1^D}}, \quad z_1 = A_1\sqrt{E_1^D \rho_1}, \tag{30}$$

the transfer matrix of the shunted PZT medium becomes

$$[T_{el,1}] = \begin{bmatrix} \tilde{c}_1(\Omega) & \dfrac{\tilde{s}_1(\Omega)}{z_1\omega} \\ -z_1\omega\dfrac{1-\tilde{c}_1^2(\Omega)}{\tilde{s}_1(\Omega)} & \tilde{c}_1(\Omega) \end{bmatrix}, \tag{31}$$

where

$$\tilde{c}_1(\Omega) = \frac{\Omega\cos(\Omega)G(\Omega) - k^2\sin(\Omega)}{\Omega G(\Omega) - k^2\sin(\Omega)},$$

$$\tilde{s}_1(\Omega) = \frac{\Omega\sin(\Omega)G(\Omega)}{\Omega G(\Omega) - k^2\sin(\Omega)}, \tag{32}$$

$$G(\Omega) = 1 + j\frac{2\xi\Omega}{\Omega_{LC,S}} - \frac{\Omega^2}{\Omega_{LC,S}^2}, \quad \Omega_{LC,S} = \frac{l\omega_{LC,S}}{c^D}.$$

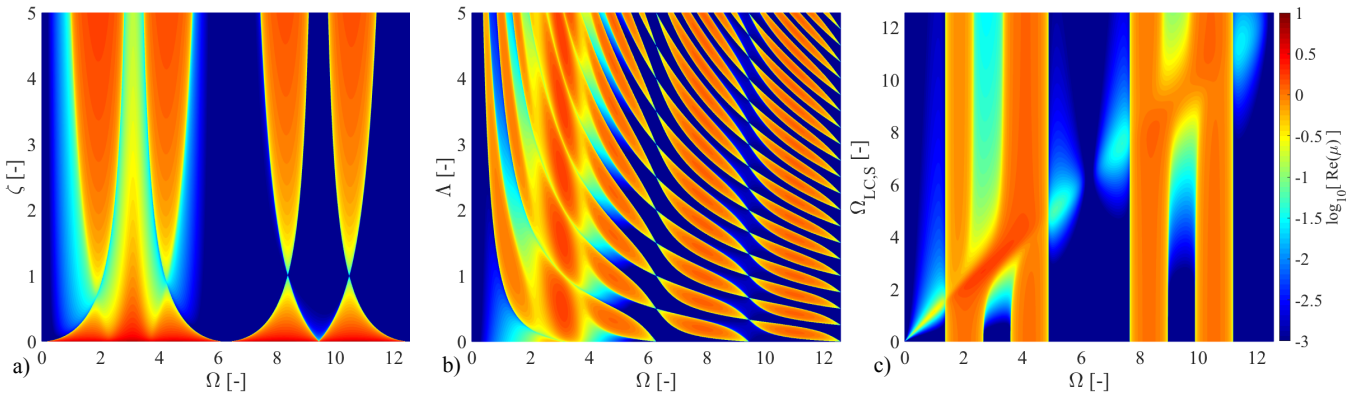

Figure 12. Non-dimensional maps obtained by the invariant equation. Color-scale represents the level of attenuation, quantified using the logarithm of the real part of the propagation constant. All the maps has $k = 0.5$ and $\xi = 0.1$: a) $\Omega - \zeta$ map with $\Omega_{LC,S} = \pi$ and $\Lambda = 0.5$; b) $\Omega - \Lambda$ map with $\Omega_{LC,S} = \pi$ and $\zeta = 0.3$; d) $\Omega - \Omega_{LC,S}$ map with $\zeta = 0.3$ and $\Lambda = 0.5$.

The trace of the full transfer matrix $[T] = [T_{el,2}][T_{el,1}]$ reads

$$I_1 = 2\cos(\Lambda\Omega)\frac{\Omega\cos(\Omega)G(\Omega) - k^2\sin(\Omega)}{\Omega G(\Omega) - k^2\sin(\Omega)} + \\ -\zeta\sin(\Lambda\Omega)\frac{\Omega\sin(\Omega)G(\Omega)}{\Omega G(\Omega) - k^2\sin(\Omega)} + \\ -\frac{1}{\zeta}\sin(\Lambda\Omega)\frac{\Omega\sin(\Omega)G(\Omega) - 2k^2[1-\cos(\Omega)]}{\Omega G(\Omega) - k^2\sin(\Omega)}, \tag{33}$$

and the propagation constant is function of six non-dimensional parameters, i.e., $\mu = \mu(\zeta, \Lambda, \Omega, \Omega_{LC,S}, \xi, k)$.

The shunting resonance frequency $\Omega_{LC,S}$ can be tuned before, inside or eventually after the first Bragg band gap as shown in Figures 10 and 11. This latter is a map with the same meaning of those in Sec. III A where the two variables are Ω and $\Omega_{LC,S}$ and the other parameters are fixed as $k = 0.5$, $\zeta = 0.3$, $\Lambda = 0.5$ and $\xi = 0$.

The first case, called Tuning A and shown in in Fig. 10a, regards the structure as a pure locally resonant metamaterial. Here, the shunting frequency is tuned before the first Bragg scattering band gap $\Omega_{LC,S} = 1$ and the plot shows the response for several damping values $\xi = 0, 0.01, 0.1$. The band gap due to the resonator provides very strong attenuation for the undamped case in a narrow bandwidth. By analyzing the sub-wavelength limit of Eq. (33), one obtains that the frequency at which the maximum attenuation occurs is well approximated by the electrical shunting frequency computed with the stress free piezoelectric capacitance ($T = 0$) $\Omega_{LC,T} = \Omega_{LC,S}\sqrt{1-k^2}$. However, since the displacements of the PZT electrodes approaches an in-phase condition for low frequencies, the PZT influence is intrinsically limited, as shown in Fig. 12. Additionally, attenuation deteriorates as damping grows, with limited advantages in terms of bandwidth, cf. Figs. 10a, 12c. To overcome these two drawbacks, it is possible to increase the impedance mismatch or the electromechanical coupling.

The other two strategies are based on the fact that the intrinsic, local electric band gap of the piezoelectric resonator can be coupled with the pure Bragg scattering of the periodic structures. The goal of the second strategy, called Tuning B and shown in Fig. 10b, is not to provide attenuation: by tuning the resonator into the first band gap, it is able to generate a pass band breaking the band gap. In this case, the shunting frequency is tuned close to the center of the first Bragg scattering band gap $\Omega_{LC,S} = 2.3$. If no shunt circuit is connected (i.e., black dashed line, short circuit condition, and the black dotted line, open circuit), band gaps are generated with Bragg scattering. When the tuning circuit is active with no damping, the first band gaps is divided in two and a pass band arises. However, as for Tuning A, in case of a high level of damping (e.g., $\xi = 0.1$) this effect does not show up anymore since damping spreads and smooth the resonator contribution in frequency.

Instead, Tuning C, whose propagation constant are given in Fig. 10c, is able to generate an extended attenuation region. It shunts at $\Omega_{LC,S} = \pi$, which is the frequency at which the PZT electrodes are exactly out of phase, hence the shunting resonance is optimally coupled to the system. In the undamped case, a very strong attenuation peak arises in between two band gaps as shown in Figs. 10c and 12. Then, raising the level of damping ($\xi = 0.01$ orange line; $\xi = 0.1$ yellow line), the attenuation peak smooths out, but again the resonator influence is spread on nearby frequencies. This results in linking two subsequent Bragg scattering band gaps in order to create a single and wider attenuation zone.

These three are the possibilities for the coexistence of Bragg scattering and a clearer understanding is provided with the maps in Figures 11 and 12 that illustrate how the real part of the propagation constant modifies in frequency when a certain parameter varies (analogue of those in Sec. III A). Figures 11 and 12c show the different tuning possibilities for two damping values, $\xi = 0, 0.1$ respectively, and with $\zeta = 0.3$ and $\Lambda = 0.5$. The three tuning strategies can be identified and analyzed here. Moreover, it is clear that the resonator influence is strongly reduced at frequency multiples of 2π (electrodes in phase), regardless of the tuning, while it is highly enhanced at π plus multiples of 2π (electrodes in phase opposition). Concerning this latter case, the maps of Figures 12a and b show

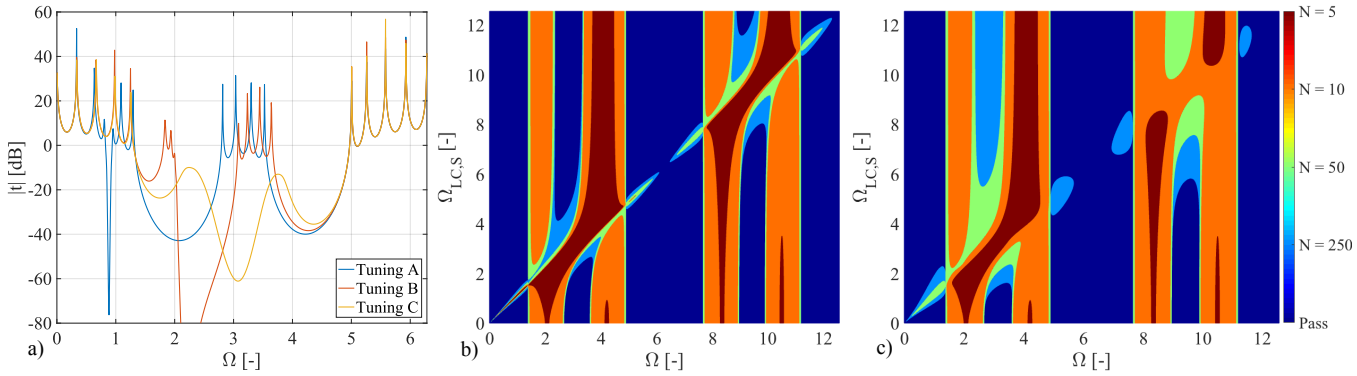

Figure 13. a) Transmissibility ratio in dB for the three tuning strategies with $k = 0.5$, $\zeta = 0.3$, $\Lambda = 0.5$, $\xi = 0.01$ (Tuning A and B), $\xi = 0.1$ (Tuning C) and $N = 5$. b-c) non-dimensional $\Omega - \Omega_{LC,T}$ maps with $\zeta = 0.3$, $\Lambda = 0.5$ and $k = 0.5$ for the finite periodic structure using the transmissibility ratio for a threshold attenuation level of -40 dB. Colors indicate the behavior for different number of unit cells and $\xi = 0.01$ in a) while $\xi = 0.10$ in b).

the effect of ζ and Λ for $\Omega_{LC,S} = \pi$ and $\xi = 0.1$. In the first one, the effect of the impedance mismatch can be observed with $\Lambda = 0.5$: at low values of ζ the shunt is able to produce the electromechanical effect while at high ones its influence is strongly reduced, and the bridging of Bragg gaps does not show up anymore. Instead, Fig. 12b shows the influence of Λ at $\zeta = 0.3$ and it can be noticed that the bridging of Bragg gaps always happens, even involving more than two Bragg band gaps. However, for increasing Λ, the bandwidth of the attenuation zone decreases and the real part of μ tends to zero for frequencies at which the second element contributes to turn the electrodes displacements in phase opposition, cf. Eq. 33. Thus, this condition might be useful for having localized resonances inside the wide attenuation zone provided by the electromechanical band gap. On the other hand, if $\Lambda < 1$, the bridging of Bragg gaps appears with its maximum extension and without any break in its band width.

Table I resumes tuning guidelines obtained by our discussion. Here, $\omega_c, 1, D = \pi c_1^D c_2/(l_1 c_2 + l_2 c_1^D)$ refers to the center of the first band gap computed via Eq. (15) and the needed shunting inductance can be retrieved as in Eq. (26). It is important to remark for Tuning A and B strategies, the damping effect is critical: the circuit resistance should be as low as possible in order to generate a band gap or break a pass band. Especially regarding Tuning A, this is one of the difficulties of resonantly shunted piezoelectric metamaterials: to achieve low frequencies, the inductance has to be increased and the resistance may ruin the attenuation level. Note also that for achieving high inductance level an active circuit is necessary that often has also a considerable internal resistance. Thus, high quality electrical circuits are necessary for these purposes.

Introducing the number of unit cells, the transmissibility ratio for the three tuning strategies is reported in Fig. 13a. The configurations are the same of Fig. 10 for 5 unit cells. Here, the deep narrow band attenuation of Tuning A at $\Omega = 0.87$, the small pass band of Tuning B centered at $\Omega = 1.9$ and the extended band gap ($1.3 < \Omega < 5$) of Tuning C can be noticed. Figures 13b and c show the effect of the number of unit cells N

Table I. Guidelines for different tuning strategies. The abbreviations a.l/h.a.p. stand for as low/high as possible (cohently with design and technical limitations) and n.i. for no importance of that parameter.

Parameter	ζ	Λ	k	$\omega_{LC,S}$	ξ
Tuning A	a.l.a.p.	n.i.	a.h.a.p.	$< \omega_{c,1,D}$	a.l.a.p.
Tuning B	”	”	”	$= \omega_{c,1,D}$	”
Tuning C	”	< 1	”	$\pi c_1^D / l_1$	$\approx 10\%$

(as in Sec. III B) varying the frequency and the electrical tuning frequency for two different values of damping. The colors identifies where the attenuation level is lower than 10^{-2}.

V. DESIGN OF A MULTI-CONFIGURATION PERIODIC STRUCTURE

This section presents an application that aims to validate the analytical prediction tools established in this paper. An ultrasonic waveguiding system, to be found in medical, non-destructive testing or imaging fields, is designed. More precisely, the proposed configuration consists of a tunable periodic structure with shunted piezoelectric inserts that is able to direct an incoming input force. Other types of non-reciprocal periodic structures may be deployed for achieving similar performances, but the current design can offer precious advantages in terms of tunability.

The periodic structure is excited in the middle with an input bandwidth approximately centered at 5 [MHz] and, thanks to the switches in the electrical circuits, this signal can be deviated to the right or left ends of the structure as shown in Fig. 14a. In the upcoming analysis, steady-states are only considered, and the latency time of switches may be safely neglected, as it can be of the order of 10[ns], which is an order of magnitude less of the time-scale of this application. Wave directing is achieved by exploiting the extended band gap generated by Bragg scattering and local resonators, which is controlled via the switches. By setting these switches on and off in the left

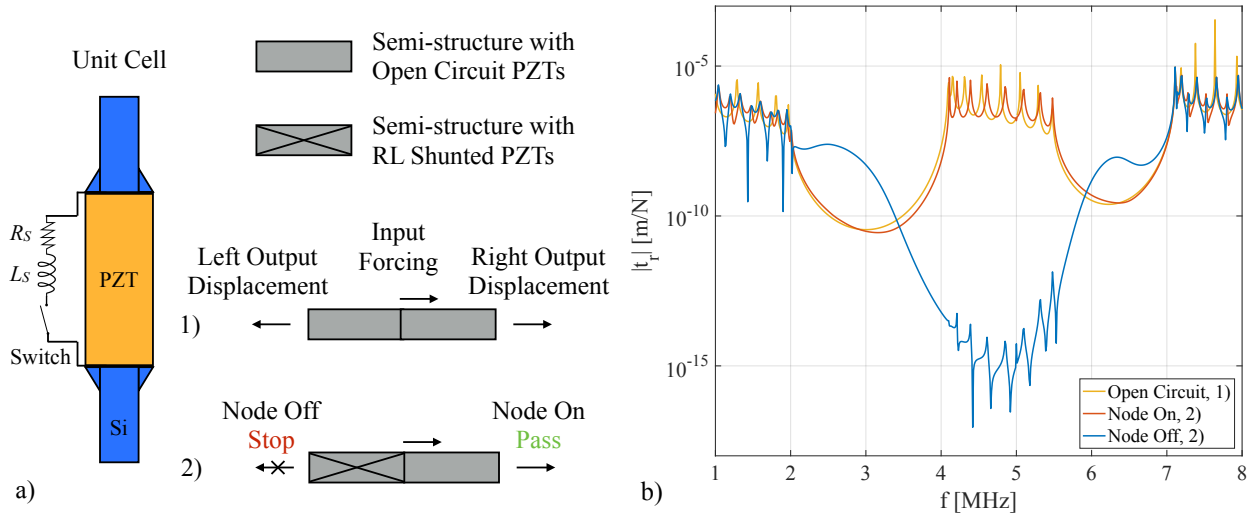

Figure 14. a) Description of the structure with its configurations and b) its analytical frequency responses obtained with the Spectral Element Method (SEM).

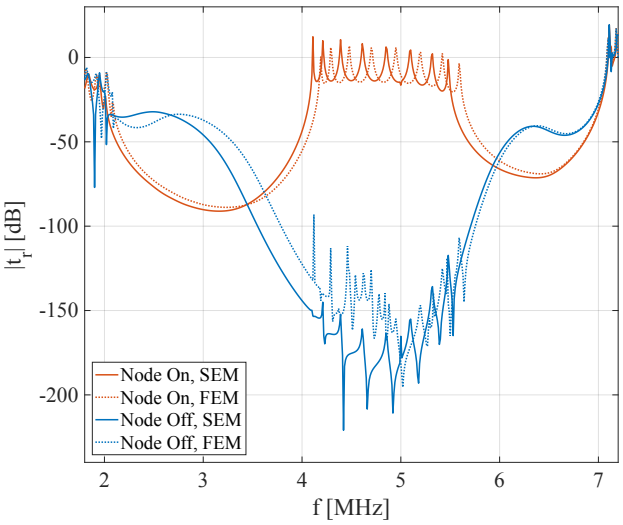

Figure 15. Transmittances of the right and left ends of analytical and numerical models (SEM, solid lines, FEM, dashed ones). With reference to Fig. 14a case 2), the blue lines refer to the right end displacement, node on, while the orange ones to the left end displacements, node off.

and right semi-structures respectively, Fig. 14a shows how input force causes a displacement in the right end while the left end one is attenuated. The yellow line illustrates the reference frequency response of either side with the whole structure having open shunt circuits (case 1). Instead, the other two lines regard the system response when the switches are closed in the left part: here, the pass band in the left end (blue line, node off) is strongly attenuated while it is still present in the right end response (orange line, node on). The signal may be also directed to the left side (i.e., switches on in the right part, off in the left one) and, eventually, the PZTs can be all shunted to attenuated wave at both sides.

Due to the developments of this paper, the design phase is pretty straightforward. First, the center of the second pass band and the tuning value of the electrical frequency $f_{LC,S}$ are both assumed to be 5 [MHz]. The materials are selected to be PZT-5H (element 1) and silicon (element 2), whose properties are $Y_1 = 107$ [GPa], $\rho_1 = 2330$ [kg/m^3], $Y_2^D = 110$ [GPa], $\rho_2 = 7500$ [kg/m^3], $k = 0.75$ [–] and $\varepsilon_{rel}^S = 1488$ [–]. The boundary conditions are supposed to be the free-free case and the out of plane thickness is uniform and imposed to be $l_1/2$ for model consistency. The optimal configurations can be selected through maps and the considerations previously illustrated. Targeting the Tuning C strategy of Sec. IV with $\zeta < 1$, $\Lambda < 1$ and $\Omega_{LC,S} = \pi$, optimization routines on the desired system responses lead to select the following other non-dimensional parameters: $\zeta = 0.3$, $\Lambda = 0.6$, $\xi = 0.1$ and $N = 16$. Therefore, the dimensional parameters are found to be: $A_1 = 1.64 \cdot 10^{-8}$ [m^2], $l_1 = 3.84 \cdot 10^{-4}$ [m], $A_2 = 0.89 \cdot 10^{-8}$ [m^2], $l_2 = 4.07 \cdot 10^{-4}$ [m], $L_S = 1.80$ [mH] ($f_{LC,S} = 5$ [MHz]), $R_S = 11.3$ [kΩ] and $L_{tot} = 12.6$ [mm].

The analytical results of this configuration are shown in Fig. 14b using the absolute value of the transmittance t_r defined as the ratio between input forcing and output displacement (see also Appendix D). These predictions are corroborated using a numerical 2D Finite Element Model (FEM), obtained using COMSOL Multiphysics® v5.2, Structural Mechanics and AC/DC modules. In order to have coherent results with the analytical model, the section mismatch has to be stiffened using chamfers (as shown in Fig. 14a): in this way, eventual transverse modes do not appear in the frequency range of interest. There is good sound between the models, except for the high attenuating region where the local resonators are tuned: here, other modes (e.g., Love waves) prevail on the ones of quasi-longitudinal wave propagation, contributing to highlight other resonance peaks and to slightly increase the overall response. Fig. 15 provides the final results and comparison between the system model. With the same colors of

Fig. 14b, solid lines represent the analytical SEM responses while dashed lines the FEM ones using a dB scale. The modest shifting of resonances is due to intrinsic modeling differences (e.g., FEM stiffening effects), but band gaps width and attenuation are very consistent overall.

VI. CONCLUSIONS

This paper analyzes the interactions of Bragg scattering and local resonators band gaps in mono-coupled infinite and finite periodic structures. Bragg scattering occurs as a result of an impedance mismatch in the unit cell, while local resonators consist of resonant shunted piezoelectric inserts.

For the case of Bragg scattering, the invariants of the transfer matrix allow to derive analytical tuning formulas and to plot non-dimensional design maps, which highlight the influence of each design parameter in the behavior of band gaps. In contrast with other literature studies, the dynamics of finite structures is also considered in detail. In this context, the transmissibility ratio constitutes the finite counterpart of the propagation constant in infinite media. Design criteria and maps are extended to the finite case, highlighting the influence of the number of unit cells and that of natural frequencies in band gap attenuation.

Resonant shunted piezoelectric inserts are introduced with a new modeling, which is valid also above the subwavelength regime. This latter shows that the shunting behavior is dominated, other than by electrical parameters, by the difference of electrodes displacements. In particular, for frequency values at which these electrodes are in phase opposition, the shunt effect is maximum, while approaches zero for in phase electrodes. Three tuning strategies for the local resonators are identified and design maps allows a thorough understanding of the effect of each parameter, including damping. Besides the classic use as a metamaterial, the local resonator can break a Bragg gap creating a pass band or, also thanks to electrical damping, make a bridge between two Bragg gaps generated an extended attenuation region.

A numerical application concludes the paper, showing and validating the established analytical tools. An ultrasonic waveguide that is able to direct an input frequency band is designed, exploiting the tunability of the extended band gap generated by the interaction of Bragg scattering and local electromechanical resonators.

Data availability. Data sharing is not applicable to this article as no new data were created or analyzed in this study.

Acknowledgements. *Competing interests.* We have no competing interests. *Funding.* We received no funding for this study.

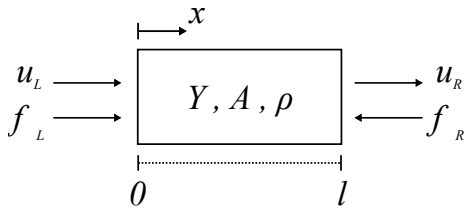

Figure 16. Representation of the rod element and sign conventions.

Appendix A: Transfer matrix for the rod element

1. Element modeling

For the rod element of length l illustrated in Fig. 16 the solution of Eq. 1 is

$$u(x;\omega) = C_1 \mathrm{e}^{-j\kappa x} + C_2 \mathrm{e}^{+j\kappa x}, \tag{A1}$$

where $j^2 = -1$, $\omega = \kappa c$ and the coefficients C_1 and C_2 have to be determined by imposing the boundary conditions. Using the sign conventions of Fig. 16, boundary displacements and forces can be defined as

$$\begin{cases} u_L = u(0,\omega), \\ u_R = u(L,\omega), \end{cases} \qquad \begin{cases} f_L = +YAu'(0;\omega), \\ f_R = -YAu'(l;\omega), \end{cases} \tag{A2}$$

where A is the cross section area. By means of Eqs (A1,A2), it is possible to obtain the dynamic stiffness matrix $[K_{el}(\omega)]$ of the rod element that relates forces with displacements at the boundaries of the element in the frequency domain

$$\begin{Bmatrix} f_L \\ f_R \end{Bmatrix} = [K_{el}(\omega)] \begin{Bmatrix} u_L \\ u_R \end{Bmatrix}, \\ [K_{el}(\omega)] = \frac{-z\omega}{\sin(\kappa l)} \begin{bmatrix} \cos(\kappa l) & -1 \\ -1 & \cos(\kappa l) \end{bmatrix} = \begin{bmatrix} k_{ll} & k_{lr} \\ k_{rl} & k_{rr} \end{bmatrix} \tag{A3}$$

where $YA\kappa = z\omega$ and $z = YA/c = A\sqrt{Y\rho}$ is the rod characteristic impedance. Thus, $[K_{el(\omega)}]$ is a symmetric, real (since there is no damping) and frequency dependent matrix, also according to the formulations of Refs. 62 and 71.

To obtain the transfer matrix, a structure of rod elements without external forcing at the nodal points[13] is assumed. The continuity and equilibrium conditions must hold between the left displacement and force of element $n+1$ and the right ones of element n,

$$u_L^{(n+1)} = u_R^{(n)}, \quad f_L^{(n+1)} = -f_R^{(n)}, \tag{A4}$$

and a state vector describing the left side is assumed $\underline{y} = [u_L \; f_L]^T$. Isolating these state variables from Eq. (A3),

$$\begin{Bmatrix} u_L^{(n+1)} \\ f_L^{(n+1)} \end{Bmatrix} = \begin{bmatrix} -k_{lr}^{-1}k_{ll} & k_{lr}^{-1} \\ k_{rr}k_{lr}^{-1}k_{ll} - k_{rl} & -k_{rr}k_{lr}^{-1} \end{bmatrix} \begin{Bmatrix} u_L^{(n)} \\ f_L^{(n)} \end{Bmatrix}, \\ \underline{y}^{(n+1)} = [T_{el}(\omega)]\underline{y}^{(n)} \tag{A5}$$

the transfer matrix is obtained[45], whose explicit form reads

$$[T_{el}(\omega)] = \begin{bmatrix} \cos(\kappa l) & \dfrac{\sin(\kappa l)}{z\omega} \\ -z\omega\sin(\kappa l) & \cos(\kappa l) \end{bmatrix}. \tag{A6}$$

Note that, in case the axial force is selected as tensile instead of compressive, the cross-diagonal elements of $[T_{el,j}]$ have opposite signs and all the elements of $[K_{el}]$ have opposite signs.

2. Invariance properties

The unit cell of a periodic structure with spatial periodicity l_c can be selected in different ways. In the bi-element case, one can choose element one on the left side and element two on the right one as shown in Fig. 1, or by stacking from left to right half of element one, element two and the reamining half of element one (i.e., a symmetric unit cell). Depending on this topological choice, the transfer matrix changes, but the matrix invariants remain the same.

Considering the state vectors $\underline{y}^{(n)} = [u(nl_c)\ f(nl_c)]^T$ and $\underline{y}_s^{(n)} = [u(s+nl_c)\ f(s+nl_c)]^T$ for $s \in (0, l_c)$, one has that

$$\underline{y}^{(n+1)} = [T(\omega)]\underline{y}^{(n)},\ \ \underline{y}_s^{(n+1)} = [\hat{T}(\omega)]\underline{y}_s^{(n)}, \tag{A7}$$

where $[T(\omega)] \neq [\hat{T}(\omega)]$ in general. The two state vectors are also related by the transfer matrix for the rod elements covering the length s

$$\underline{y}_s^{(n)} = [T_s(\omega)]\underline{y}^{(n)}, \tag{A8}$$

which holds for any positive or negative interger n due to structural periodicity. Using Eq. (A8), one obtains

$$\underline{y}^{(n+1)} = [T_s(\omega)]^{-1}[\hat{T}(\omega)][T_s(\omega)]\underline{y}^{(n)}, \tag{A9}$$

which states that, being $\underline{y}^{(n)}$ and s arbitrary, $[\hat{T}(\omega)]$ and $[T(\omega)]$ are similar matrices, hence they have the same eigenvalues.

Appendix B: Proof of Proposition II.1

The following lemma is necessary for the proof of Proposition II.1. Interestingly, the same result is stated without formal proof in Ref. 45.

Lemma B.1. *Let* $[T] \in \mathbb{R}^{2\times 2}$ *be such that* $\det([T]) = 1$ *and indicate its eigenvalues with* $e^{\pm\mu}$*. Then, it holds that*

$$[T]^N = \frac{a}{2}\Big([T] + [T]^{-1}\Big) + \frac{b}{2}\Big([T] - [T]^{-1}\Big), \tag{B1}$$

where $a = \cosh(N\mu)/\cosh(\mu)$ *and* $b = \sinh(N\mu)/\sinh(\mu)$.

Proof. Firstly, let $[T]$ be a diagonalizable matrix. Hence,

$$\begin{aligned} [T] &= [S]^{-1}[D][S], \\ [T]^{-1} &= [S]^{-1}[D]^{-1}[S], \end{aligned} \tag{B2}$$

where $[D]$ is a diagonal 2×2 matrix containing the eigenvalues of $[T]$ and $[S]$ is a transformation matrix. Then,

$$[T]^N = [S]^{-1}[D]^N[S], \tag{B3}$$

Using the notation $ch = \cosh(\mu)$, $sh = \sinh(\mu)$, $ch_N = \cosh(N\mu)$ and $sh_N = \sinh(N\mu)$, one can find that

$$\begin{aligned} [T] + [T]^{-1} &= [S]^{-1}\begin{bmatrix} 2ch & 0 \\ 0 & 2ch \end{bmatrix}[S], \\ [T] - [T]^{-1} &= [S]^{-1}\begin{bmatrix} 2sh & 0 \\ 0 & -2sh \end{bmatrix}[S], \end{aligned} \tag{B4}$$

that are valid also for the analogue case of $[T]^N$ using ch_N and sh_N instead of ch and sh respectively. By noting that

$$\begin{aligned} &([T]^N + [T]^{-N}) + ([T]^N - [T]^{-N}) = \\ &= [S]^{-1}\begin{bmatrix} 2(ch_N + sh_N) & 0 \\ 0 & 2(ch_N - sh_N) \end{bmatrix}[S], \end{aligned} \tag{B5}$$

it is possible to achieve

$$[T]^N = ch_N[S]^{-1}\begin{bmatrix} 1 & 0 \\ 0 & 1 \end{bmatrix}[S] + sh_N[S]^{-1}\begin{bmatrix} 1 & 0 \\ 0 & -1 \end{bmatrix}[S]\ . \tag{B6}$$

Rearranging Eq. (B4) as

$$\begin{aligned} [S]^{-1} &= \frac{1}{2ch}([T] + [T]^{-1})[S]^{-1}\begin{bmatrix} 1 & 0 \\ 0 & 1 \end{bmatrix}, \\ [S]^{-1} &= \frac{1}{2sh}([T] - [T]^{-1})[S]^{-1}\begin{bmatrix} 1 & 0 \\ 0 & -1 \end{bmatrix}, \end{aligned} \tag{B7}$$

and using these results in (B6), one obtains $[T]^N$ as claimed. If $[T]$ is not diagonalizable, then its eigenvalues are either equal to $+1$ or -1 and $[T]$ is similar to a upper triangular Jordan block. For this latter matrix, one can easily verify that the same formula holds and hence, by similarity, Eq. (B1) is valid for every $[T] \in \mathbb{R}^{2\times 2}$ with unitary determinant. □

Proof of Proposition II.1. For a sequence of N unit cells the relationship between the state vectors is

$$\underline{y}(N_l c) = [T(\omega)]^N \underline{y}(0). \tag{B8}$$

The link between the state vector variables and the forces and displacement of the periodic structure at the left and right sides (*ls* and *rs* as shown in Fig. 2) is

$$\begin{aligned} u(N_l c) &= u_{rs}, \quad u(0) = u_{ls}, \\ f(N_l c) &= -f_{rs}, \ \ f(0) = f_{ls}, \\ \begin{Bmatrix} u_{rs} \\ -f_{rs} \end{Bmatrix} &= [T(\omega)]^N \begin{Bmatrix} u_{ls} \\ f_{ls} \end{Bmatrix}, \end{aligned} \tag{B9}$$

where the negative is needed for structural equilibrium (see also Appendix A). When coupling the periodic structure with the external medium, continuity has to be guaranteed for the displacements

$$u_{rs} = u_t(Nl_c) = U_t,\ \ u_{ls} = u_i(0) + u_r(0) = U_i + U_r, \tag{B10}$$

while equilibrium must be imposed with the axial force of the external medium, for which it holds that $f_e = Y_e A_e du/dx$

$$\begin{array}{ll} f_{rs} + f_e(Nl_c) = 0 & \rightarrow \; f_{rs} = j\omega z_e U_t, \\ f_{ls} + f_e(0) = 0 & \rightarrow \; f_{ls} = j\omega z_e (U_i - U_r), \end{array} \tag{B11}$$

Denoting $t_{N,lm}$ the elements (l-th row, m-th column) of the matrix $[T(\omega)]^N$, from Eqs. (B9-B11) one can derive

$$\begin{cases} U_t = (t_{N,11} + j\omega z_e t_{N,12})U_i + (t_{N,11} - j\omega z_e t_{N,12})U_r, \\ U_t = (-t_{N,22} + j\frac{t_{N,21}}{\omega z_e})U_i + (t_{N,22} + j\frac{t_{N,21}}{\omega z_e})U_r, \end{cases} \tag{B12}$$

and the ratios t and r can be computed

$$\begin{cases} r \;\; = \dfrac{U_r}{U_i} = \dfrac{t_{N,11} + j\omega z_e t_{N,12} - j\frac{t_{N,21}}{\omega z_e} + t_{N,22}}{-t_{N,11} + j\omega z_e t_{N,12} + j\frac{t_{N,21}}{\omega z_e} + t_{N,22}}, \\ t \;\; = \dfrac{U_t}{U_i} = \dfrac{2(t_{N,11}t_{N,22} - t_{N,12}t_{N,21})}{-t_{N,11} + j\omega z_e t_{N,12} + j\frac{t_{N,21}}{\omega z_e} + t_{N,22}}, \end{cases} \tag{B13}$$

It is worth noticing that the numerator of t in Eq. (B13) is equal to the determinant of matrix $[T(\omega)]^N$.

Using Lemma B.1 and the formula

$$[T(\omega)]^{-1} = \begin{bmatrix} t_{22} & -t_{12} \\ -t_{21} & t_{11} \end{bmatrix}, \tag{B14}$$

the N-th power of transfer matrix can be written as

$$[T(\omega)]^N = \begin{bmatrix} T_N + U_{N-1}\dfrac{t_{11} - t_{22}}{2} & U_{N-1}t_{12} \\ U_{N-1}t_{21} & T_N - U_{N-1}\dfrac{t_{11} - t_{22}}{2} \end{bmatrix}, \tag{B15}$$

where T_N and U_{N-1} depend on the first invariant of $[T]$ as

$$\begin{aligned} T_N = T_N\left(\frac{I_1}{2}\right) = \cosh(N\mu), \;\; \cosh(\mu) = \frac{I_1}{2}, \\ U_{N-1} = U_{N-1}\left(\frac{I_1}{2}\right) = \frac{\sinh(N\mu)}{\sinh(\mu)}, \end{aligned} \tag{B16}$$

and they are respectively the Chebyshev polynomials[66] of first T and second U kind of degree N and $N-1$. Since $\det([T]^N) = \det([T])^N = 1$, the transmissibility ratio then reads

$$t = \frac{2}{\left[-(t_{11} - t_{22}) + j\left(\omega z_e t_{12} + \dfrac{t_{21}}{\omega z_e}\right)\right]\dfrac{\sinh(N\mu)}{\sinh(\mu)}} \tag{B17}$$

as claimed. □

According to Eq. (4), the attenuation per element α takes the form

$$\begin{aligned} \alpha &= \frac{1}{N}\log\left(\left|\frac{\sinh(N\mu)}{\sinh(\mu)}\right|\sigma_e\right), \\ \sigma_e &= \sqrt{\left(\frac{t_{11} - t_{22}}{2}\right)^2 + \left(\frac{\omega z_e t_{12}}{2} + \frac{t_{12}}{2\omega z_e}\right)^2}, \end{aligned} \tag{B18}$$

for which it holds that

$$\begin{aligned} \lim_{N\to\infty}\alpha \; &= \lim_{N\to\infty}\frac{1}{N}\log\left(\left|\frac{\sinh(N\mu)}{\sinh(\mu)}\right|\sigma_e\right) \\ &= \lim_{N\to\infty}\frac{1}{N}\log\left(\mathrm{e}^{N\mathrm{Re}(\mu)}\left|\frac{1 - \mathrm{e}^{-2N\mu}}{2\sinh(\mu)}\right|\sigma_e\right) \\ &= \mathrm{Re}(\mu), \end{aligned} \tag{B19}$$

where the identity $\sinh(N\mu) = \mathrm{e}^{N\mu}(1 - \mathrm{e}^{-2N\mu})/2$ has been exploited for the computation of this limit. This theoretical evidence establish the connection between infinite and finite media, as anticipated in Sec. II.

Appendix C: An approximate formula for Bragg gap centers

The maximum of the real part of μ happens when the first invariant of $[T]$ is a local maximum or minimum since the inverse hyperbolic cosine is a monotonic function. Note that, in a stop band, for $\mathrm{Tr}([T]) > 0$, $\mu = \mathrm{acosh}[\mathrm{Tr}([T])]$, while for $\mathrm{Tr}([T]) < 0$, $\mu = \mathrm{acosh}[|\mathrm{Tr}([T])|] + j\pi$. So, whenever μ is purely real and $\mathrm{Tr}([T])$ has a stationary point in frequency, a center of the band gap is expected. Then

$$\begin{aligned} \frac{\partial I_1}{\partial \Omega} = \; & -(1+\Lambda)\left[1 + \left(\frac{\zeta}{2} + \frac{1}{2\zeta}\right)\right]\sin[\Omega(1+\Lambda)] + \\ & -(1-\Lambda)\left[1 - \left(\frac{\zeta}{2} + \frac{1}{2\zeta}\right)\right]\sin[\Omega(1-\Lambda)] \end{aligned} \tag{C1}$$

and imposing this derivative to be zero is again a nonlinear equation for which no exact general solution can be obtained. We may take some limiting values with Λ whose effect is stronger in the solution of this equation. For $\Lambda = 1$, the second term in the right hand side of Eq. (C1) is zero, so it remains $\sin(2\Omega) = 0$ and the band gap centers are $\Omega = m\pi/2$ for $m \in \mathbb{N}$. Instead, for $\Lambda >> 1$, we have $2\Lambda\sin(\Lambda\Omega) = 0$ so that $\Omega = m\pi/\Lambda$, while for $\Lambda << 1$, the equation to solve becomes $2\sin(\Omega) = 0$, resulting in $\Omega = m\pi$. In every case, the band gap center location in frequency is only dependent on the Λ parameter. An approximated function complying with these limiting values is that expressed in Eq. (15).

Appendix D: Natural frequencies and frequency responses for finite periodic structures

In order to obtain natural frequencies and frequency responses, one can use the Spectral Element Method[71] (SEM).

Table II. Natural frequencies of finite mono-coupled periodic systems whose boundary conditions are, for the left and right ends respectively, free-free (FF), clamped-clamped (CC), clamped-free (CF) and free-clamped (FC).

Boundary conditions	Equations
FF: $f_{ls} = f_{rs} = 0 \rightarrow t_{N,21} = 0$	$U_{N-1} = 0$ & $t_{21} = 0$
CC: $u_{ls} = u_{rs} = 0 \rightarrow t_{N,12} = 0$	$U_{N-1} = 0$ & $t_{12} = 0$
FC: $f_{ls} = u_{rs} = 0 \rightarrow t_{N,11} = 0$	$2T_N + U_{N-1}(t_{11} - t_{22}) = 0$
CF: $u_{ls} = f_{rs} = 0 \rightarrow t_{N,22} = 0$	$2T_N - U_{N-1}(t_{11} - t_{22}) = 0$

Starting from the dynamic stiffness matrix of a single element $[K_{el}(\omega)]$ reported in Eq. (A3), all the element matrices can be assembled and the boundary conditions imposed in order to compute the global dynamic stiffness matrix $[K_g(\omega)]$

$$\underline{f}_g = [K_g(\omega)]\underline{u}_g, \tag{D1}$$

where $\underline{f}_g$ and $\underline{u}_g$ are the vectors respectively containing the forces and displacements at the global degrees of freedom of the structure. Hence, the the global dynamic stiffness matrix serves for computing natural frequency and modes as frequency response functions. However, the transfer matrix can help again in deriving analytical formulations for solving these problems and avoiding numerical routines. With the usual nomenclature, Eq. (B9) can be made explicit

$$\begin{Bmatrix} u_{rs} \\ f_{rs} \end{Bmatrix} = \begin{bmatrix} +t_{N,11} & +t_{N,12} \\ -t_{N,21} & -t_{N,22} \end{bmatrix} \begin{Bmatrix} u_{ls} \\ f_{ls} \end{Bmatrix}, \tag{D2}$$

and so, thanks to these equations relating the two boundaries of the system, the natural frequencies can be computed according to the boundary conditions, for which the main cases are reported in Table II. The free-free and clamped-clamped cases have $N-1$ frequencies that are determined by the first invariant only. From Table II, it is also clear that the free-free or clamped-clamped natural frequencies of the periodic rod are equivalent in the majority except for a countable infinity of frequencies. As discussed in Sec. IV B, most of natural frequencies lie in pass band, but some (those related to the equations $t_{21} = 0$ or $t_{12} = 0$) can appear inside band gaps. Moreover, some peculiar frequency response functions can be analytically calculated from Eq. (D2). By imposing here that $f_{rs} = 0$, one obtains the transmittance t_r of a forced-free structure

$$\begin{aligned} t_r &= \frac{u_{rs}}{f_{ls}} = -\frac{1}{t_{N,21}} = \frac{\bar{t}_r}{\omega z_1}, \\ \bar{t}_r &= \frac{1}{(\sin(\Omega)\cos(\Lambda\Omega) + \zeta\cos(\Omega)\sin(\Lambda\Omega))\,U_{N-1}}. \end{aligned} \tag{D3}$$

REFERENCES

[1] L. Brillouin, *Propagation in Periodic Structures: Electric Filters and Crystal Lattices* (Dover Publications, 1953).

[2] D. Mead, "Wave propagation in continuous periodic structures: research contributions from southampton, 1964-1995," Journal of Sound and Vibration **190**, 495–524 (1996).

[3] M. Maldovan, "Sound and heat revolutions in phononics," Nature **503**, 209–217 (2013).

[4] V. Laude, *Phononic Crystals* (De Gruyter, 2015).

[5] Y.-F. Wang, Y.-Z. Wang, B. Wu, W. Chen, and Y.-S. Wang, "Tunable and active phononic crystals and metamaterials," Applied Mechanics Reviews **72** (2020), 10.1115/1.4046222, 040801.

[6] J. Joannopoulos, S. Johnson, J. Winn, and R. Meade, *Photonic Crystals: Molding the Flow of Light* (Princeton University Press, 2011).

[7] M. Maldovan and E. Thomas, "Simultaneous localization of phonons and photons in two-dimensional periodic structures," Applied Physics Letters **88** (2006).

[8] A. Safavi-Naeini, J. Hill, S. Meenehan, J. Chan, S. Gröblacher, and O. Painter, "Two-dimensional phononic-photonic band gap optomechanical crystal cavity," Physical Review Letters **112** (2014).

[9] C. Elachi, "Waves in active and passive periodic structures: a review," Proceeding of the IEEE **133** (2011).

[10] W. L. Barnes, A. Dereux, and T. W. Ebbesen, "Surface plasmon subwavelength optics," Nature **424**, 824–830 (2013).

[11] C. Kittel, *Introduction to Solid State Physics, 8th Ed.* (Wiley, 2004).

[12] D. Mead, "Plates with regular stiffening in acoustic media: vibration and radiation," The Journal of the Acoustic Society of America **88**, 391–401 (1990).

[13] M. Hussein, M. Leamy, and M. Ruzzene, "Dynamics of phononic materials and structures: historical origins, recent progress, and future outlook," Applied Mechanics Reviews **66**, 1–38 (2014).

[14] L. D'Alessandro, E. Belloni, R. Ardito, A. Corigliano, and F. Braghin, "Modeling and experimental verification of an ultra-wide bandgap in 3d phononic crystal," Applied Physical Letters **109**, 221907 (2016).

[15] S. Hedayatrasa, K. Abhary, M. Uddin, and C. Ng, "Optimum design of phononic crystal perforated plate structures for widest bandgap of fundamental guided wave modes and maximized in-plane stiffness," Journal of the Mechanics and Physics of Solids **89**, 31–58 (2016).

[16] A. Krushynska, K. V.G., and M. Geers, "Towards optimal design of locally resonant acoustic metamaterials," Journal of the Mechanics and Physics of Solids **71**, 179–196 (2014).

[17] F. Casadei and K. Bertoldi, "Wave propagation in beams with periodic arrays of airfoil-shaped resonating units," Journal of Sound and Vibration **333**, 6532–6547 (2014).

[18] S. Krödel, N. Thomé, and C. Daraio, "Wide band-gap seismic metastructures," Extreme Mechanics Letters , 111–117.

[19] C. Sugino, S. Leadenham, M. Ruzzene, and A. Erturk, "On the mechanism of bandgap formation in locally resonant finite elastic metamaterials," Journal of Applied Physics **120**, 134501 (2016).

[20] A. Spadoni, M. Ruzzene, and K. Cunefare, "Vibration and wave propagation control of plates with periodic arrays of shunted piezoelectric patches," Journal of Intelligent Material Systems and Structures **20**, 979–990 (2009).

[21] L. Airoldi, M. Senesi, and M. Ruzzene, "Piezoelectric superlattices and shunted periodic arrays as tunable periodic structures and metamaterials," in *Wave Propagation in Linear and Nonlinear Periodic Media: Analysis and Applications*, edited by F. Romeo and M. Ruzzene (Springer Vienna, 2012) pp. 33–108.

[22] Y. Chen, G. Hu, and G. Huang, "A hybrid elastic metamaterial with negative mass density and tunable bending stiffness," Journal of the Mechanics and Physics of Solids **105**, 179–198 (2017).

[23] B. Mace and E. Manconi, "Wave motion and dispersion phenomena: veering, locking and strong coupling effects," Journal of the Acoustical Society of America **131**, 1015–1028 (2011).

[24] E. Flores Parra, A. Bergamini, B. Lossouarn, B. Van Damme, M. Cenedese, and P. Ermanni, "Bandgap control with local and interconnected lc piezoelectric shunts," Applied Physics Letters **111**, 111902 (2017).

[25] G. Trainiti, Y. Xia, J. Marconi, G. Cazzulani, A. Erturk, and M. Ruzzene, "Time-periodic stiffness modulation in elastic metamaterials for selective wave filtering: Theory and experiment," Phys. Rev. Lett. **122**, 124301 (2019).

[26] J. Marconi, E. Riva, M. Di Ronco, G. Cazzulani, F. Braghin, and M. Ruzzene, "Experimental observation of nonreciprocal band gaps in a space-time-modulated beam using a shunted piezoelectric array," Phys.

Rev. Applied **13**, 031001 (2020).
[27] J. Hsu, "Local resonances-induced low-frequency band gaps in two-dimensional phononic crystal slabs with periodic stepped resonators," Journal of Physics D: Applied Physics **44**, 055401 (2011).
[28] C. Croënne, E. Lee, H. Hefei, and J. Page, "Band gaps in phononic crystals: generation mechanisms and interaction effects," AIP Advances **1**, 041401 (2011).
[29] N. Kaina, M. Fink, and G. Lerosey, "Composite media mixing bragg and local resonances for highly attenuating and broad bandgaps," Scientific Reports **3**, 3240 (2013).
[30] L. Raghavan and A. Phani, "Local resonance bandgaps in periodic media: Theory and experiment," The Journal of the Acoustical Society of America **134**, 1950–1959 (2013), https://doi.org/10.1121/1.4817894.
[31] B. Yuan, V. Humphrey, J. Wen, and X. Wen, "On the coupling of resonance and bragg scattering effects in three-dimensional locally resonant sonic materials," Ultrasonics **53**, 1332 – 1343 (2013).
[32] Y. Chen and L. Wang, "Periodic co-continuous acoustic metamaterials with overlapping locally resonant and bragg band gaps," Applied Physics Letters **105**, 191907 (2014).
[33] B. Sharma and C. Sun, "Local resonance and bragg bandgaps in sandwich beams containing periodically inserted resonators," Journal of Sound and Vibration **364**, 133 – 146 (2016).
[34] D. Colquitt, A. Colombi, R. Craster, P. Roux, and S. Guenneau, "Seismic metasurfaces: Sub-wavelength resonators and rayleigh wave interaction," Journal of the Mechanics and Physics of Solids **99**, 379 – 393 (2017).
[35] A. Krushynska, F. Miniaci, M. and. Bosia, and N. Pugno, "Coupling local resonance with bragg band gaps in single-phase mechanical metamaterials," Extreme Mechanics Letters **12**, 30 – 36 (2017), frontiers in Mechanical Metamaterials.
[36] Y. Tian, J. Wu, H. Li, C. Gu, Z. Yang, Z. Zhao, and K. Lu, "Elastic wave propagation in the elastic metamaterials containing parallel multi-resonators," Journal of Physics D: Applied Physics **52**, 395301 (2019).
[37] M. Moscatelli, R. Ardito, L. Driemeier, and C. Comi, "Band-gap structure in two- and three-dimensional cellular locally resonant materials," Journal of Sound and Vibration **454**, 73 – 84 (2019).
[38] D. Mead, "Wave propagation and natural modes in periodic systems: I. mono-coupled systems," Journal of Sound and Vibration **40**, 1–18 (1975).
[39] M. Ruzzene and A. Baz, "Attenuation and localization of wave propagation in periodic rods using shape memory inserts," ASME Journal of Vibration and Acoustics **9**, 805–816 (2000).
[40] S. Asiri, A. Baz, and D. Pines, "Periodic struts for gearbox support system," Journal of Vibration and Control **11**, 709–741 (2005).
[41] I. Malfanti, A. Taschin, P. Bartolini, B. Bonello, and R. Torre, "Propagation of acoustic surface waves on a phononic surface investigated by transient reflecting grating spectroscopy," Journal of the Mechanics and Physics of Solids **59**, 2370 – 2381 (2011).
[42] G. Yang, J. Du, and J. Wang, "Propagation of surface acoustic wave in one-dimensional piezoelectric phononic crystals," Proceedings of the 2014 Symposium on Piezoelectricity, Acoustic Waves, and Device Applications , 366–369 (2014).
[43] D. Richards and D. Pines, "Passive reduction of gear mesh vibration using a periodic drive shaft," Journal of Sound and Vibration **264**, 317–342 (2003).
[44] Y. Song, J. Wen, D. Yu, and X. Wen, "Analysis and enhancement of torsional vibration stopbands in a periodic shaft system," Journal of Physics D: Applied Physics **46** (2013).
[45] M. Faulkner and D. Hong, "Free vibrations of a mono-coupled periodic system," Journal of Sound and Vibration **99**, 29–42 (1985).
[46] O. Thorp, M. Ruzzene, and A. Baz, "Attenuation and localization of wave propagation in rods with periodic shunted piezoelectric patches," Smart Material and Structures **10**, 979–989 (2001).
[47] L. Airoldi and M. Ruzzene, "Design of tunable acoustic metamaterials through periodic arrays of resonant shunted piezos," New Journal of Physics **13** (2011).
[48] J. Xu, X. Zhang, and R. Yan, "Experimental demonstration of the wave attenuation capability of a piezoelectric metamaterial beam by using correlation for signal processing," Journal of Applied Physics **128**, 174903 (2020).
[49] C. Shengbing, W. Jihong, W. Gang, Y. Dianlong, and W. Xisen, "Improved modeling of rods with periodic arrays of shunted piezoelectric patches," Journal of Intelligent Material Systems and Structures **23**, 1613–1621 (2012).
[50] E. Pestel and F. Leckie, *Matrix Methods in Elastomechanics* (McGraw-Hill Inc, New York, 1963).
[51] M. Brun, S. Guenneau, A. Movchan, and D. Bigoni, "Dynamics of structural interfaces: filtering and focussing effects for elastic waves," Journal of the Mechanics and Physics of Solids **58**, 1212–1224 (2010).
[52] E. G. Williams, P. Roux, M. Rupin, and W. A. Kuperman, "Theory of multiresonant metamaterials for A_0 lamb waves," Physical Review B **91**, 104307 (2015).
[53] C. Lim and X. Xu, "Symplectic elasticity: theory and applications," Applied Mechanics Reviews **63** (2011).
[54] M. A. de Gosson, *Symplectic Methods in Harmonic Analysis and in Mathematical Physics* (Birkäuser, 2011).
[55] F. Bloch, "Über die quantenmechanik der elektronen in kristallgittern," Zeitschrift fur Physik **52**, 555–600 (1929).
[56] D. Mead, "A general theory of harmonic wave propagation in linear periodic systems with multiple coupling," Journal of Sound and Vibration **27**, 235–260 (1973).
[57] F. Romeo and A. Luongo, "Invariant representation of propagation properties for bi-coupled periodic structures," Journal of Sound and Vibration **257**, 869–886 (2002).
[58] G. Carta and M. Brun, "Bloch-Floquet waves in flexural systems with continuous and discrete elements," Mechanics of Materials **87**, 11–26 (2015).
[59] J. Wei and M. Petyt, "A method of analyzing finite periodic structures, part 1: theory and examples," Journal of Sound and Vibration **202**, 555–569 (1997).
[60] D. Griffiths and C. Steinke, "Waves in locally periodic media," American Journal of Physics **69**, 137–154 (2001).
[61] W. Jung, Z. Gu, and A. Baz, "Mechanical filtering characteristics of passive periodic engine mount," Finite Elements in Analysis and Design **46**, 685–697 (2010).
[62] J. Doyle, *Wave Propagation in Structures* (Springer-Verlag, 1989).
[63] F. Farzbod and M. Leamy, "Analysis of Bloch's method and the propagation technique in periodic structures," Journal of Vibration and Acoustics **133** (2011).
[64] F. Romeo, "Map-based approaches for periodic structures," in *Wave Propagation in Linear and Nonlinear Periodic Media: Analysis and Applications*, edited by F. Romeo and M. Ruzzene (Springer Vienna, 2012) pp. 161–256.
[65] M. Born and E. Wolf, *Principles of Optics: Electromagnetic Theory of Propagation, Interference and Diffraction of Light* (Pergamon Press, 1980).
[66] J. Mason and D. Handscomb, *Chebyshev Polynomials* (Chapman and Hall/CRC, 2002).
[67] D. Miu, *Mechatronics - Electromechanics and Contromechanics,* (Springer-Verlag, 1993).
[68] A. Preumont, *Mechatronics - Dynamics of Electromechanical and Piezoelectric Systems* (G.M.L. Gladwell, Ed. Springer Netherlands, 2006).
[69] Q. Qin, *Advanced Mechanics of Piezoelectricity* (Springer, 2013).
[70] D. Hopkins and G. Gazonas, *Wave propagation in second-order nonlinear piezoelectric media* (Army Research Laboratory, 2011).
[71] U. Lee, *Spectral Element Method in Structural Dynamics* (Wiley, 2009).